

Experimental observation of edge-dependent quantum pseudospin Hall effect

Huanhuan Yang¹,¹ Lingling Song,¹ Yunshan Cao,¹ X. R. Wang,^{2,*} and Peng Yan^{1,†}

¹*School of Electronic Science and Engineering and State Key Laboratory of Electronic Thin Films and Integrated Devices, University of Electronic Science and Technology of China, Chengdu 610054, China*

²*Physics Department, The Hong Kong University of Science and Technology, Clear Water Bay, Kowloon, Hong Kong*



(Received 12 January 2021; revised 16 July 2021; accepted 13 December 2021; published 22 December 2021)

It is conventional wisdom that the helical edge states of a quantum spin Hall (QSH) insulator are particularly stable due to the topological protection of time-reversal symmetry. Here, we report experimental observation of an edge-dependent quantum (pseudo)spin Hall effect by employing two Kekulé electric circuits with molecule-zigzag and partially bearded edges, where the chirality of the circulating current in the unit cell mimics the electron spin. We observe a helicity flipping of the topological in-gap modes emerging in opposite parameter regions for the two edge geometries. Experimental findings are interpreted in terms of the mirror winding number defined in the unit cell, the choice of which exclusively depends on the edge shape. Our work offers a deeper understanding of the boundary effect on the QSH phase and paves the way for studying the spin-dependent topological physics in electric circuits.

DOI: [10.1103/PhysRevB.104.235427](https://doi.org/10.1103/PhysRevB.104.235427)

I. INTRODUCTION

A paradigm in the topological band insulator family [1,2] is the quantum spin Hall (QSH) insulator, which has an insulating gap in the bulk but supports gapless helical states at the boundary [3–6]. QSH insulators are characterized by the topological \mathbb{Z}_2 invariant, defined in the presence of time-reversal symmetry. Because of the symmetry protection, the helical edge states are robust against the electronic backscattering [5–9], ushering in a new era in spintronics and quantum computing [10–13]. Counterintuitively, Freney *et al.* recently reported an edge-dependent topology in artificial Kekulé lattices [14]. The mechanism is that the edge geometries of samples determine the choice of the unit cell and further dictate the value of topological invariants [15–17]. It is intriguing to ask if there is any spin-resolved topological effect related to the edge shape of graphenelike materials [18,19] or other topological insulators [20,21]. This question motivates us to address theoretically and experimentally the edge-dependent quantum (pseudo)spin Hall effect.

Recently, the topoelectrical circuit sprang up as a powerful platform to study fundamental topological physics [22–31] since simple inductor-capacitor (LC) networks can fully simulate the tight-binding model in condensed-matter physics. In this work, we fabricate two kinds of Kekulé LC circuits with molecule-zigzag and partially bearded edges (see Fig. 1). By measuring the node-ground impedance and monitoring the spatiotemporal voltage signal propagation, we observe the quantum pseudospin Hall effect emerging in opposite parameter regions with flipped helicities for the two different edge terminations, where the chirality of the circulating current in

the unit cell mimics the spin. A quantized mirror winding number is proposed to explain our experimental findings.

This paper is organized as follows. The circuit model and main results are displayed in Sec. II, in which we present the experimental observations of an edge-dependent quantum pseudospin Hall effect by employing two Kekulé electric circuits, accompanied by the numerical calculations. In Sec. III, we explain these findings by evaluating the mirror winding number defined in the unit cell. In Sec. IV, we clarify the meaning of pseudospin and map the circuit Hamiltonian to the Bernevig-Hughes-Zhang model. Conclusions are drawn in Sec. V.

II. CIRCUIT MODEL AND MAIN RESULTS

We consider two finite-size artificial Kekulé circuits with molecule-zigzag and partially bearded edge terminations, as shown in Figs. 1(a) and 1(b), respectively. The circuits consist of two types of capacitors, C_A and C_B , and an inductor L . The response of the circuit at frequency ω is given by Kirchhoff's law:

$$I_a(\omega) = \sum_b J_{ab}(\omega)V_b(\omega), \quad (1)$$

where I_a is the external current flowing into node a , V_b is the voltage of node b , and $J_{ab}(\omega) = i\omega[-C_{ab} + \delta_{ab}(\sum_n C_{an} - \frac{1}{\omega^2 L_a})]$ is the circuit Laplacian, with C_{ab} being the capacitance between nodes a and b and the sum being taken over all nearest-neighbor nodes. Based on Eq. (1), we explicitly express the circuit Laplacians $J_I(\omega)$ and $J_{II}(\omega)$ of the two circuits in Figs. 1(a) and 1(b). At the resonant frequency $\omega_0 = 1/\sqrt{(2C_A + C_B)L}$, the diagonal elements of the circuit Laplacians vanish.

Two printed circuit boards with different edge geometries are displayed in Figs. 2(a) and 2(b). In experiments, we adopt

*Corresponding author: phxwan@ust.hk

†Corresponding author: yan@uestc.edu.cn

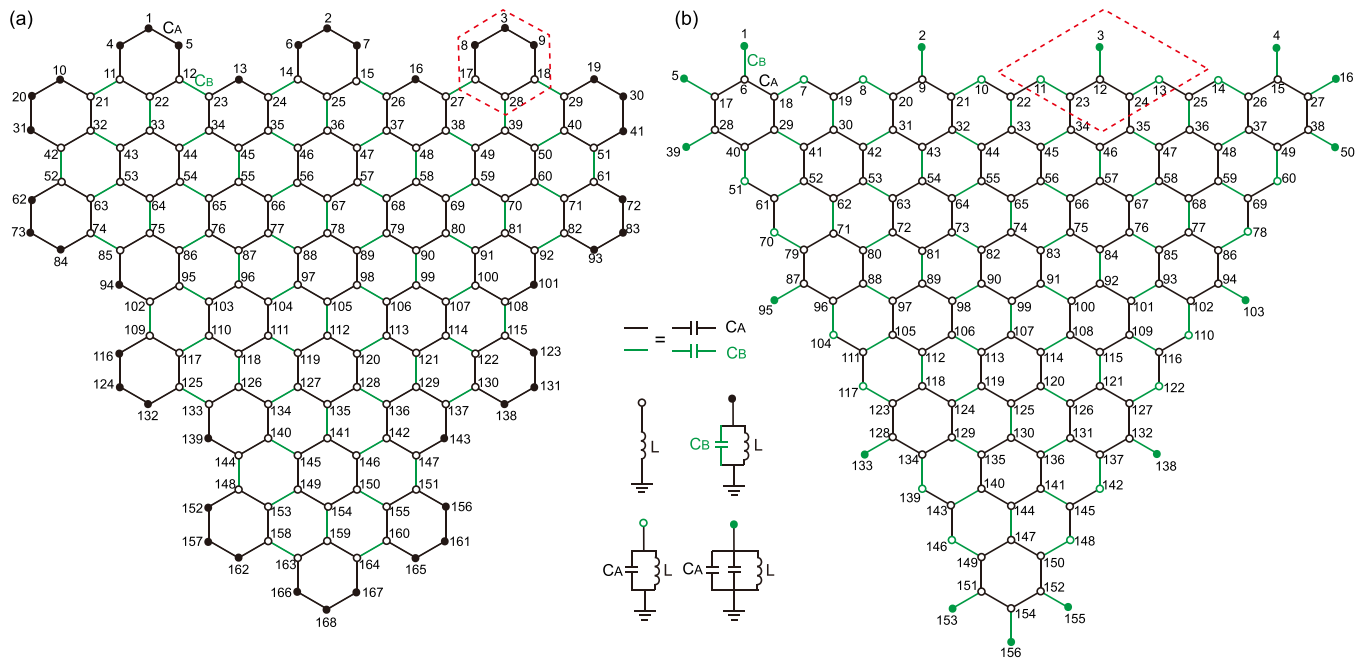


FIG. 1. Illustration of two artificial Kekulé LC circuits with (a) molecule-zigzag and (b) partially bearded edge terminations. Each node is grounded by inductors and capacitors with the configuration shown in the inset. The dashed red hexagon and rhombus represent the appropriate unit cells for the two different edge shapes.

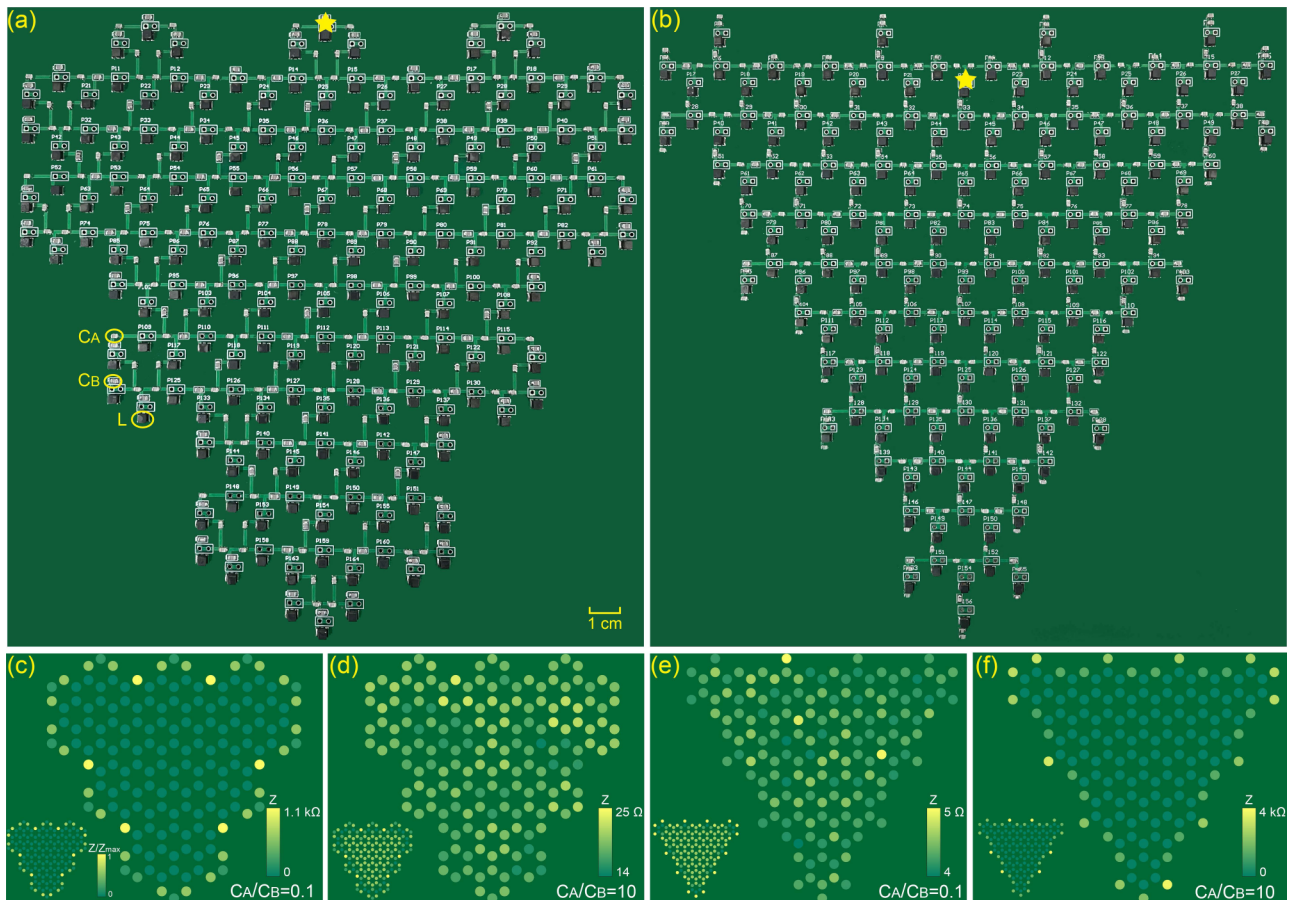


FIG. 2. Printed circuit boards with (a) molecule-zigzag and (b) partially bearded edges. Yellow stars label the position of signal sources in the voltage measurements. (c)–(f) Experimental measurements of the spatial distribution of impedance between each node and the ground. Insets: numerical results.

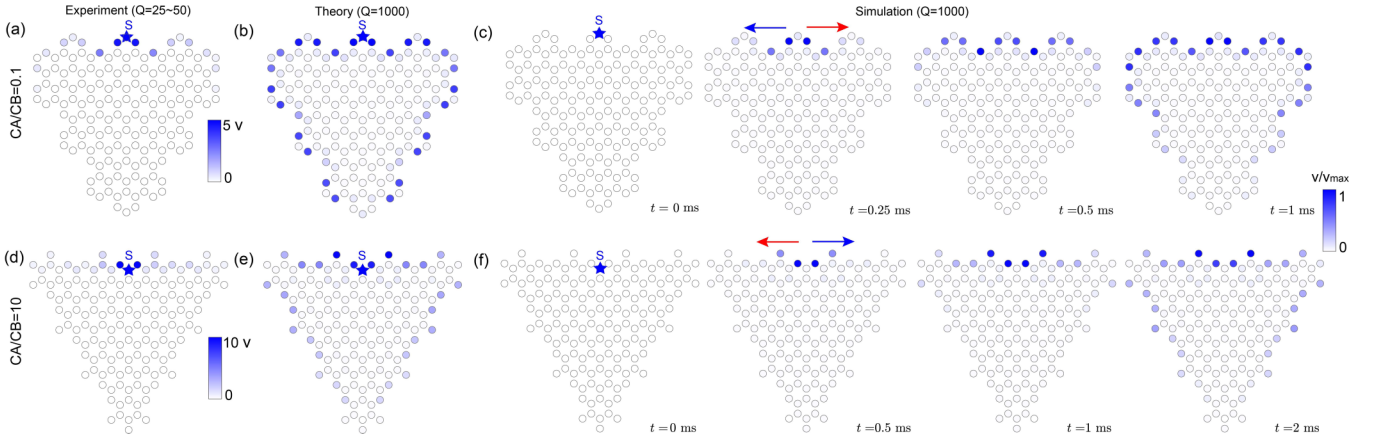


FIG. 3. Experimental measurements of the steady-state amplitude of the voltage oscillation in devices with (a) molecule-zigzag ($C_A/C_B = 0.1$) and (d) partially bearded ($C_A/C_B = 10$) edges. (b) and (e) Theoretical calculation with $Q = 1000$. (c) and (f) Snapshots of the propagating voltage. The blue star labels the position of the signal source, and the red and blue arrows represent the propagation direction of the voltage with up and down pseudospins, respectively.

$C_A = 1$ nF, $C_B = 10$ or 0.1 nF, and $L = 39$ μ H (all circuit elements have a 2% tolerance; see Appendix A), with the resonant frequency being $\omega_0/2\pi = 1/[2\pi\sqrt{(2C_A + C_B)L}] = 232.65$ or 556.13 kHz, respectively.

We measure the distributions of impedance between each node and the ground with the impedance analyzer (Keysight E4990A), and the results are plotted in Figs. 2(c)–2(f). For devices with a molecule-zigzag edge at $C_A/C_B = 0.1$ [Fig. 2(c)] and a partially bearded edge at $C_A/C_B = 10$ [Fig. 2(f)], we observe that the impedance concentrates on the sample edge, the value of which is larger than 1000 Ω , indicating the existence of edge states (Appendix A). Theoretically, the impedance between nodes a and b is given by [28]

$$Z_{ab} = \frac{V_a - V_b}{I_{ab}} = \sum_n \frac{|\psi_{n,a} - \psi_{n,b}|^2}{j_n}, \quad (2)$$

where $|\psi_{n,a} - \psi_{n,b}|$ is the amplitude difference between the a and b nodes of the n th eigenstate and j_n is the n th eigenvalue. We plot the numerical results in the insets of Figs. 2(c)–2(f), showing excellent agreement with the experimental measurements.

It is known that the QSH insulator allows bidirectional propagation states along the boundary. However, we cannot directly observe the time-resolved wave dynamics by measuring the impedance. To solve this problem, we monitor and record the spatiotemporal voltage signal in the circuits. Specifically, we impose a sinusoidal voltage signal $v(t) = v_0 \sin(\omega_0 t)$ with amplitude $v_0 = 5$ V at the node labeled by blue stars in Figs. 3(a) and 3(b) by an arbitrary function generator (GW AFG-3022) and then measure the steady-state voltage distribution using an oscilloscope (Keysight MSOX3024A). We indeed observe a strong voltage response along both directions of the device edge. However, the voltage signal decays very fast away from the voltage source because of the low quality factor ($Q = 25$ – 50) of the inductors. To overcome this issue, we add active elements (negative resistance) in the edge nodes to improve the Q factor (see

Appendix B) and directly observe a much longer propagation distance of the edge states [see Figs. 3(a) and 3(d)]. In Figs. 3(b) and 3(e), we also plot the theoretical steady-state voltage distributions with higher Q factor inductors ($Q = 1000$) for comparison.

To see the propagation details of the edge states, we perform circuit simulations with LTSPICE [32] and record the voltage of all nodes. For the two edge states along molecule-zigzag and partially bearded boundaries, the voltage signals propagate in both directions along the edge, as displayed in Figs. 3(c) and 3(f), accompanied by the helicity flipping indicated by red and blue arrows (see the analysis below).

To explain the experimental results, we numerically calculate the band structure of the circuits. By diagonalizing the circuit Laplacians $J_I(\omega)$ and $J_{II}(\omega)$, we obtain the admittance spectrum j_n and the corresponding wave functions $\psi_{n,m}$, as shown in Fig. 4. For circuits with a molecule-zigzag edge, with $C_A/C_B = 0.1$, isolated states emerge in the gap of the bulk admittance spectrum which correspond to the edge states, as shown in Fig. 4(a). When $C_A/C_B = 10$, only bulk states are identified [see Fig. 4(b)]. For circuits with a partially bearded edge, on the contrary, we find that the edge states emerge in the opposite capacitance ratio, i.e., $C_A/C_B = 10$, as displayed in Fig. 4(c). For $C_A/C_B = 0.1$, one can observe only the bulk states [see Fig. 4(d)]. These results are fully consistent with our experimental observations.

III. TOPOLOGICAL INVARIANT

Next, we analyze the origin of the bidirectional edge states. First of all, we can exclude the Tamm-Shockley mechanism [33,34], which predicts that the periodicity breaking of the crystal potential at the boundary can lead to the formation of a conducting surface/edge state. However, this surface/edge state is trivial because it is sensitive to impurities, defects, and disorder (see Appendix A), which is not compatible with our experimental findings. There thus must be a topological

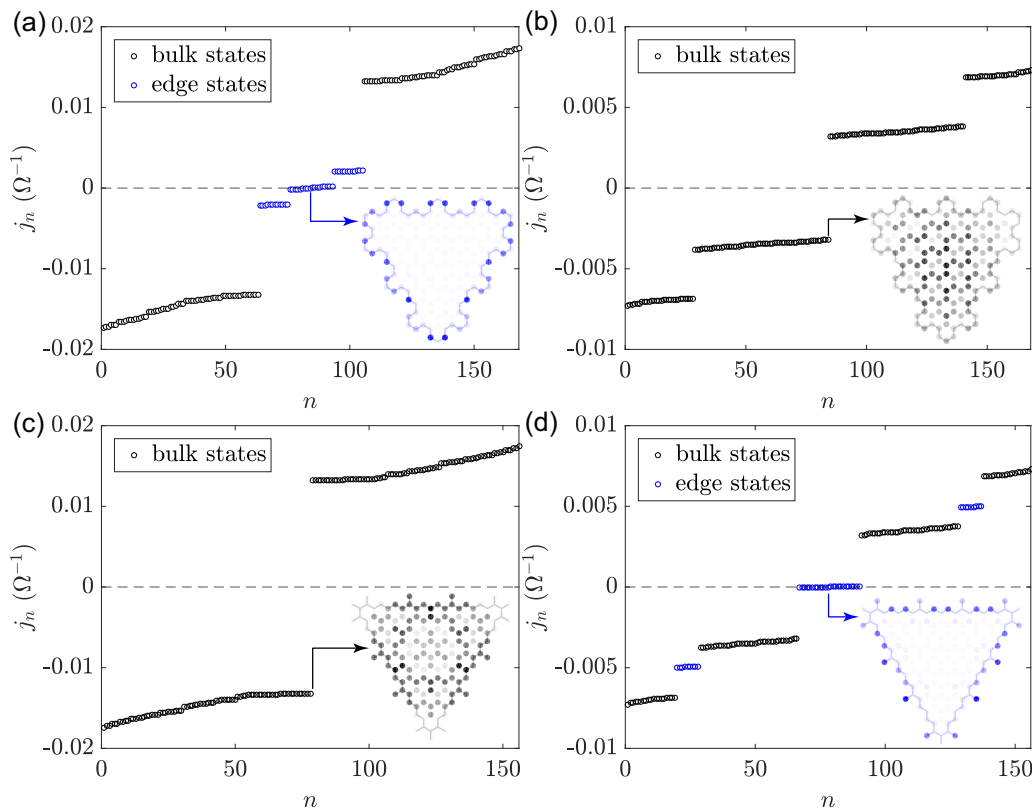


FIG. 4. The blue and black dots denote the edge states and bulk states, respectively. Insets: spatial distribution of wave functions, with the number of states indicated by the arrows. (a) and (b) Molecule-zigzag edge with $C_A/C_B = 0.1$ and $C_A/C_B = 10$. (c) and (d) Partially bearded edge with $C_A/C_B = 0.1$ and $C_A/C_B = 10$.

reason for the emerging bidirectional edge states we observed. To justify this point of view, we employ the mirror winding number (n_+, n_-) defined in the unit cell [15],

$$n_{\pm} = -\frac{1}{2\pi} \oint \frac{d}{dk_{\perp}} \arg(\det Q_{k_{\perp}^{\pm}}) dk_{\perp}, \quad (3)$$

where

$$Q_{k_{\perp}^{\pm}} = \begin{pmatrix} C_B \bar{Y}^2 & \sqrt{2}C_A \\ \sqrt{2}C_A & C_A + C_B Y \end{pmatrix}, \quad Q_{k_{\perp}^{-}} = C_B Y - C_A$$

for molecule-zigzag edge termination and

$$Q_{k_{\perp}^{\pm}} = \begin{pmatrix} C_B & \sqrt{2}C_A \\ \sqrt{2}C_A \bar{Y} & C_B + C_A Y \end{pmatrix}, \quad Q_{k_{\perp}^{-}} = C_B - C_A Y$$

for partially bearded edge termination. Here $Y = e^{i\frac{3}{2}k_{\perp}}$, with k_{\perp} being the projection of wave vector \mathbf{k} to the \hat{y} direction. The choice of the unit cell depends on the shape of the sample edge. As shown in Figs. 1(a) and 1(b), the dashed red hexagon and rhombus represent the unit cells for the two different edge geometries. For the circuit with the molecule-zigzag edge, we obtain $(n_+, n_-) = (1, -1)$ when $C_A/C_B < 1$ and $(0, 0)$ when $C_A/C_B > 1$. Therefore, we can observe the topological edge states when $C_A/C_B < 1$. For the circuit with the partially bearded edge, the situation is inverted: $(n_+, n_-) = (0, 0)$ when $C_A/C_B < 1$ and $(1, -1)$ when $C_A/C_B > 1$, indi-

cating that the topological edge states arise in the region of $C_A/C_B > 1$ (see Appendix C).

IV. PSEUDOSPIN AND MAPPING TO THE BERNEVIG-HUGHES-ZHANG MODEL

Figures 5(a) and 5(d) show two infinitely long ribbons with molecule-zigzag and partially bearded edges. For the ribbon with the molecule-zigzag edge, in the case of $C_A/C_B < 1$, we find three isolated modes in the band gap [see Fig. 5(b)]. The red and blue spectra represent the helical edge states with opposite group velocities. We introduce the circulating bond currents inside the unit cell: $i_{m \rightarrow n} = i(c_n^{\dagger} c_m - c_m^{\dagger} c_n)$, with c_n and c_n^{\dagger} being the annihilation and creation operators, respectively, at site n [35–37], with their flow direction plotted on the right in Figs. 5(a) and 5(d). Interestingly, we find that the chiralities of the circulating current are opposite for the in-gap red and blue bands, which mimics the electron spin-up and spin-down states, respectively, and the two modes are independent of each other (see Appendixes D and E). This observation is reminiscent of the spin-momentum locking in the QSH effect. The brown line denotes the flat band localized in the bottom zigzag edge of the ribbon [38]. Moreover, we find that Kirchhoff's law can be mapped to the Schrödinger equation (see Appendix F), and the underlying physics of our circuit model should be identical to the quantum-mechanical one. Indeed, by experimentally measuring the crossing

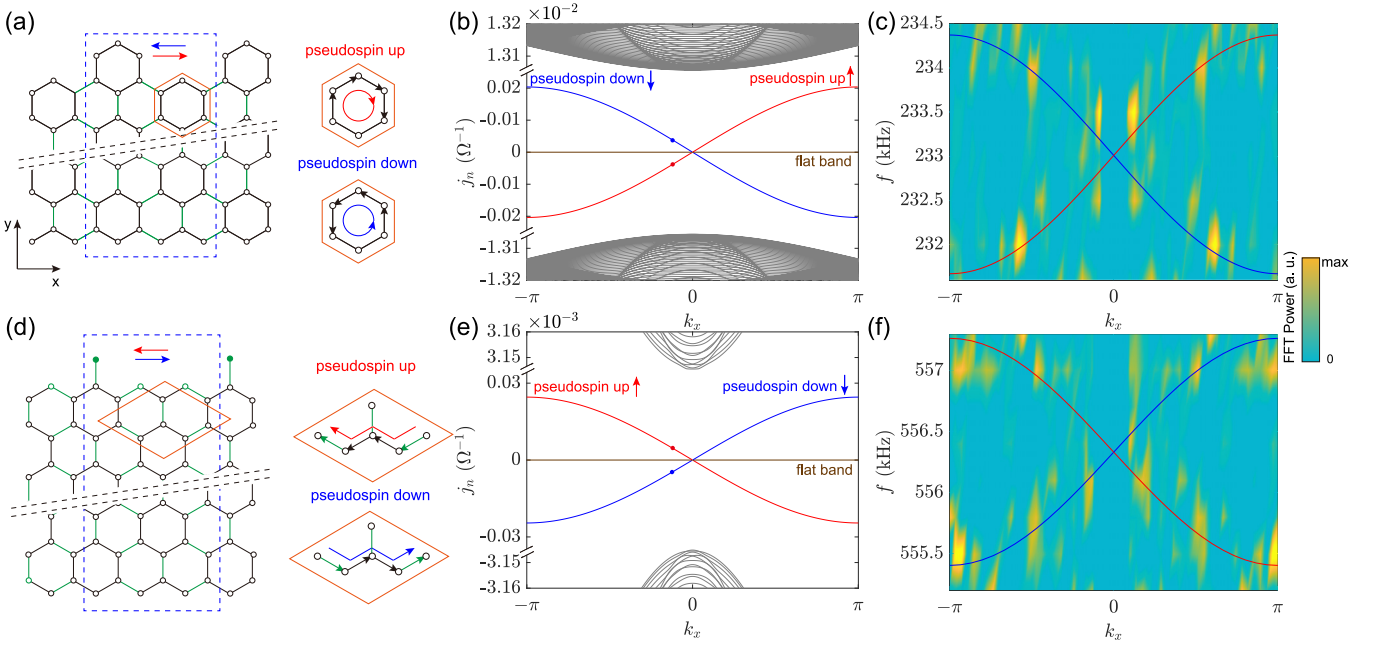


FIG. 5. (a) Schematic plot of a ribbon with a molecule-zigzag edge (top) and a graphene-zigzag edge (bottom). The ribbon is periodic along the \hat{x} direction and contains 40 unit cells along the \hat{y} direction. Insets: the pseudospin is denoted by the chirality of the circulating current in the unit cell. (b) Calculated admittance spectrum of the ribbon with capacitor ratio $C_A/C_B = 0.1$. Red and blue lines represent the dispersive edge states with pseudospin up and down counterpropagating along the top edge. The brown line denotes the localized mode in the bottom edge. (d) Illustration of a ribbon with a partially bearded edge (top) and a graphene-zigzag edge (bottom). (e) Calculated admittance spectrum with capacitor ratio $C_A/C_B = 10$. (c) and (f) Measured band structure in the frequency domain.

spectrum in the frequency domain [see Fig. 5(c)], we observe good agreement with the admittance spectrum. For $C_A/C_B > 1$, there is no in-gap energy spectrum expect for the flat band (see Appendix F). For the ribbon with a partially bearded edge, the edge modes with flipped helicity, however, only appear in the region of $C_A/C_B > 1$ [see Figs. 5(e) and 5(f)].

To understand the origin of the helicity flipping, we reduce the six-band circuit Laplacian to the four-band Bernevig-Hughes-Zhang (BHZ) model originally proposed for HgTe quantum wells [5,6]. To this end, we express $J_{ab}(\omega) = i\mathcal{H}_{ab}(\omega)$, in which $\mathcal{H}(\omega)$ can be viewed as a Hermitian tight-binding Hamiltonian. Taking the molecule-zigzag unit cell as an example, one can write the Hamiltonian of an infinite Kekulé circuit at resonance as

$$\mathcal{H} = -\omega_0 C_A \sum_{\langle i,j \rangle} c_i^\dagger c_j - \omega_0 C_B \sum_{\langle i',j' \rangle} c_{i'}^\dagger c_{j'}, \quad (4)$$

where $\langle i,j \rangle$ and $\langle i',j' \rangle$ run over nearest-neighboring sites inside and between hexagonal unit cells, respectively. Diagonalizing Hamiltonian (4), we obtain six bands, two of which are high-energy bands with the phase transition point $C_A/C_B = 1$ at the low-energy Γ point. We further note that the high-energy parts are irrelevant to the topological phase transition. By performing a unitary transformation $\mathcal{H}' = U^\dagger \mathcal{H} U$ on \mathcal{H} around the Γ point, we separate the two high-energy orbits and obtain the low-energy effective BHZ-type Hamiltonian as follows (see Appendix D):

$$\mathcal{H}_{\text{eff}}(\mathbf{k}) = -\omega_0 \begin{pmatrix} H(\mathbf{k}) & 0 \\ 0 & H^*(-\mathbf{k}) \end{pmatrix}, \quad (5)$$

with

$$H(\mathbf{k}) = \begin{pmatrix} M - Bk^2 & Ak_- \\ A^*k_+ & -M + Bk^2 \end{pmatrix},$$

where $M = C_B - C_A$, $A = -\frac{3}{2}iC_B$, $B = \frac{9}{4}C_B$, $k^2 = k_x^2 + k_y^2$, and $k_{\pm} = k_x \pm ik_y$.

For the circuit with a partially bearded unit cell, we obtain a similar low-energy effective Hamiltonian, but with $M = C_A - C_B$. The sign of the parameter M is opposite for the two edge geometries, leading to the helicity flipping of the edge states in the opposite parameter regions based on the band inversion mechanism. Here the parameter M can be interpreted as an effective spin-orbit coupling (SOC) associated with the pseudospin, which is different from the intrinsic one originating from the relativistic effect. However, the SOC in the circuit is tunable and can be very large, enabling the observation of the quantum pseudospin Hall states at room temperature.

V. CONCLUSION

In summary, we reported an edge-dependent quantum pseudospin Hall effect in topoelectric circuits. We showed that the pseudospin is represented by the chirality of the circulating current in the unit cell. Through the impedance measurement and spatiotemporal voltage signal detection assisted by circuit simulations, we directly identified the helical nature of the edge states. The emerging topological phases were characterized by mirror winding numbers, which depend on the shape of the device edge. Our work uncovered the importance of the edge geometry in the QSH effect and opens a pathway to using

circuits to simulate the spin-dependent topological physics, which may inspire research in other solid-state systems and stimulate applications in information transmission, patterned imaging, and computing in the future (see Appendix G).

ACKNOWLEDGMENTS

This work was supported by the National Natural Science Foundation of China (Grants No. 12074057, No. 11604041, and No. 11704060). X.R.W. acknowledges the financial support of Hong Kong RGC (Grants No. 16302321, No. 16301518, and No. 16301619).

APPENDIX A: THE INFLUENCE OF THE TOLERANCES OF CIRCUIT ELEMENTS

In this Appendix, we investigate the impact of tolerances of the circuit elements. Considering a simple parallel LC unit with different tolerances [see the inset in Fig. 6(a)], we choose $\langle L \rangle = 39 \mu\text{H}$, $\langle C \rangle = C_A + 2C_B = 12 \text{ nF}$ and calculate its impedance. As shown in Fig. 6(a), the impedance decreases with larger fluctuations as the tolerance increases (we averaged the results after 10^4 realizations of uniformly distributed disorders). Then, we introduce disorders to the molecule-zigzag circuit. We calculate the average impedance after 10^4 realizations of uniformly distributed disorders [see Figs. 6(b)–6(e)] and find that the impedance is still well confined to the edge but its magnitude decreases. The real circuit elements always have large production-related tolerances in capacitance and inductance (about 10%). To demonstrate a

clean result, we select the circuit components with small tolerance (2%).

APPENDIX B: IMPROVING THE Q FACTOR OF INDUCTORS WITH THE NEGATIVE RESISTANCES

In this Appendix, we improve the Q factor of inductors by introducing the active elements (negative resistances) to the circuits. In passive experiments, the voltage signal decays very quickly during the propagation, which is limited by the quality factor (Q factor) of the inductor. The quality factor is defined as $Q = \omega L/r$, with r being the unavoidable loss of material. To compensate the dissipation, we improve the Q factor of the inductor by adding a series of active elements (negative resistance) to the boundary nodes, as shown in Fig. 7(a).

For an ideal operational amplifier, $i_+ = 0$, $i_- = 0$, and $u_d = 0$ (most modern amplifiers have large gains and input impedances, so the analysis is feasible in a real circuit). According to Ohm's law, we obtain

$$v_{\text{in}} - v_o = iR, \quad v_o = \frac{R_A + R_B}{R_B} v_{\text{in}}. \quad (\text{B1})$$

Combining these two equations, we have

$$\frac{v_{\text{in}}}{i} = -\frac{R_A}{R_B} R. \quad (\text{B2})$$

When $R_A = R_B$, the network is equivalent to a negative resistance due to $v_{\text{in}} = i(-R)$. With these active elements, we measure the voltage propagation again. We compare the

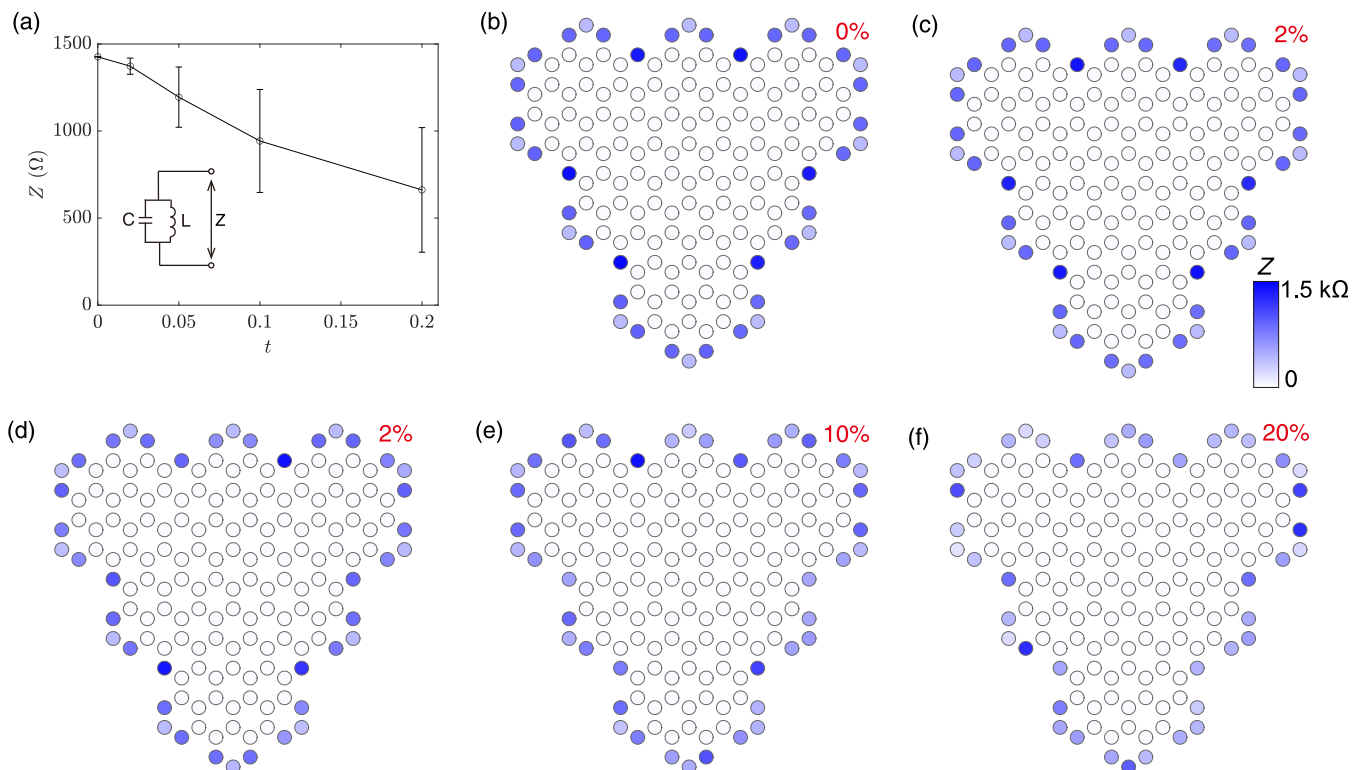


FIG. 6. (a) Impedance and its fluctuation for different tolerances of the circuit elements. t is the maximal intensity of the uniformly distributed disorder. (b)–(f) The distribution of the impedance for different tolerances.

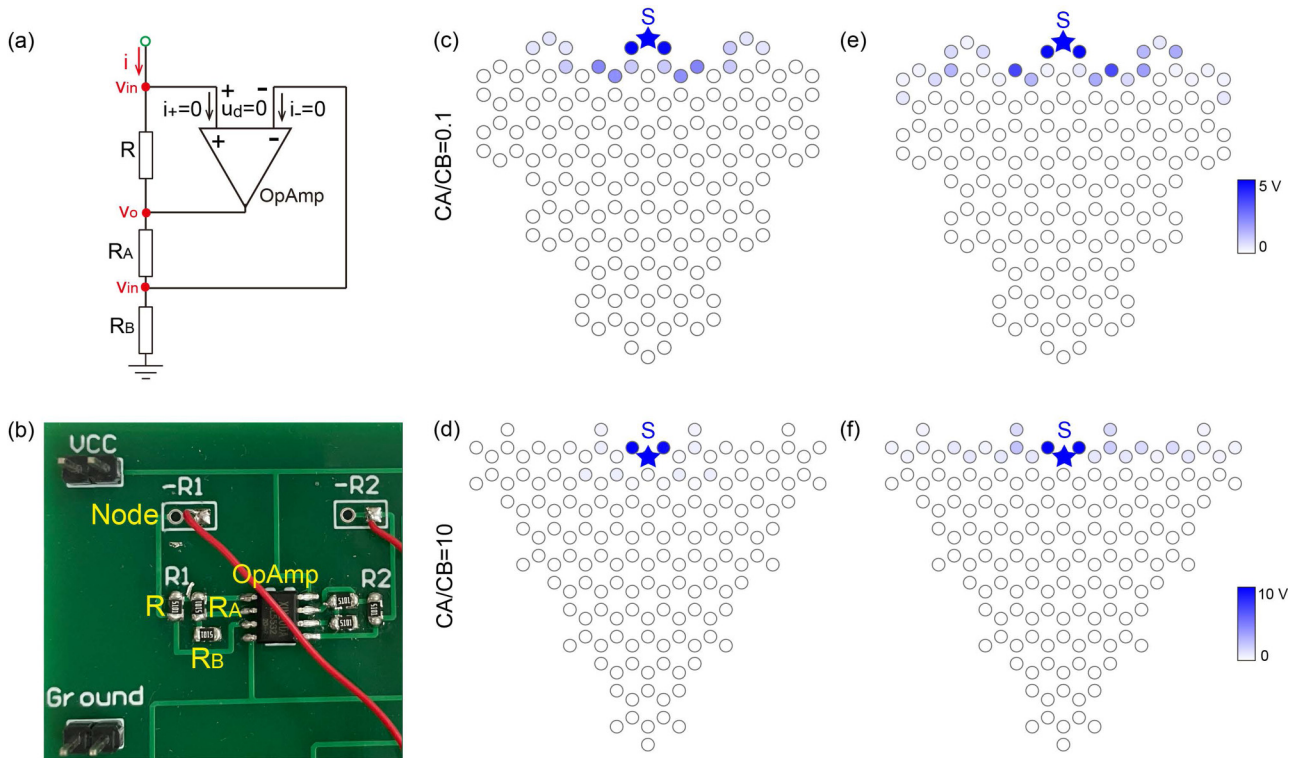


FIG. 7. (a) The schematic diagram and (b) photograph of the printed circuit board of negative resistances. The distribution of the amplitude of the voltage signal (c), (d) without and (e), (f) with negative resistances.

distribution of the amplitude of the voltage signal without and with negative resistance, shown in Figs. 7(c), 7(d) and 7(e), 7(f), respectively. In the presence of negative resistances, the voltage signal can propagate over a larger distance along the edge, especially for the partially bearded case.

We also analyze the validity of the experimental setup (connecting the negative resistances to only the boundary nodes) with a comparison for two cases: (i) negative resistances associated with only the boundary nodes and (ii) negative resistances associated with all nodes. The results are shown in the Fig. 8, from which we observe that (i) the negative resistances can slow down the decay of the voltage signal [compare the results in Figs. 8(a) and 8(b)] and (ii) one can hardly distinguish the results with the negative resistances

connected to only the edge nodes [Fig. 8(b)] and to all nodes [Fig. 8(c)] because the edge mode is exponentially decaying to the bulk. We therefore conclude that connecting the negative resistance to only the boundary nodes is reasonable, which also lowers the complexity of our experiments (since we can use fewer electrical elements).

APPENDIX C: MIRROR WINDING NUMBER

In this Appendix, we calculate the topological invariant i.e., mirror winding number, to characterize the helical edge states. With the appropriate unit cells in Fig. 9 (unit cell I for the circuit with a molecule-zigzag edge and unit cell II for the circuit with a partially bearded edge), we can write the

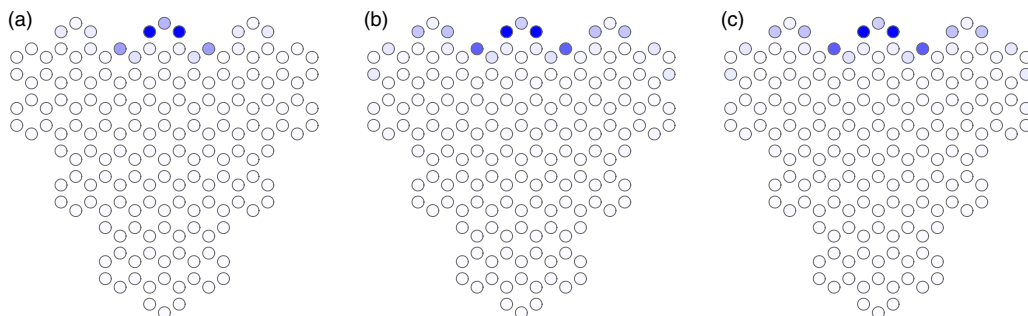


FIG. 8. Propagation of the voltage signal for different Q -factor inductors. (a) $Q = 50$ for all nodes (without negative resistance). (b) $Q = 50$ for bulk nodes, and $Q = 100$ for boundary nodes (with negative resistance to only edge nodes). (c) $Q = 100$ for all nodes (with negative resistance to all nodes).

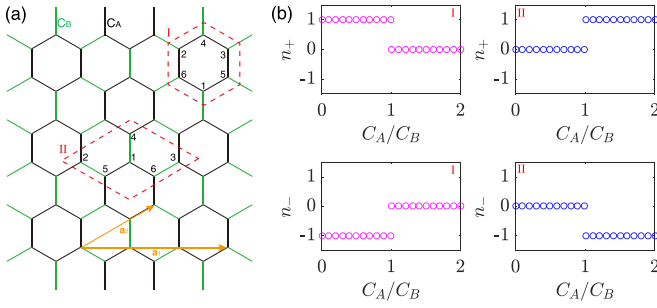


FIG. 9. (a) Appropriate unit cells for molecule-zigzag and partially bearded edges. The orange arrows label the two basic vectors. (b) The mirror winding numbers (n_+ , n_-) as a function of the capacitance ratio C_A/C_B .

Hamiltonian of an infinite Kekulé circuit as

$$\mathcal{H} = \omega \begin{pmatrix} h_0 & 0 & 0 & & & \\ 0 & h_0 & 0 & & -Q_{\mathbf{k}} & \\ 0 & 0 & h_0 & & & \\ & -Q_{\mathbf{k}}^\dagger & & h_0 & 0 & 0 \\ & & & 0 & h_0 & 0 \\ & & & 0 & 0 & h_0 \end{pmatrix}, \quad (\text{C1})$$

with the matrix elements $h_0 = 2C_A + C_B - 1/(\omega^2 L)$,

$$Q_{\mathbf{k}}^I = \begin{pmatrix} C_B X \bar{Y}^2 & C_A & C_A \\ C_A & C_B \bar{X} Y & C_A \\ C_A & C_A & C_B Y \end{pmatrix} \quad (\text{C2})$$

for the molecule-zigzag edge, where $X = e^{i\mathbf{k} \cdot \mathbf{a}_1}$ and $Y = e^{i\mathbf{k} \cdot \mathbf{a}_2}$, with $\mathbf{a}_1 = 3\sqrt{3}\hat{x}$ and $\mathbf{a}_2 = \frac{3\sqrt{3}}{2}\hat{x} + \frac{3}{2}\hat{y}$ being the two basic vectors, and

$$Q_{\mathbf{k}}^{II} = \begin{pmatrix} C_B & C_A & C_A \\ C_A \bar{Y} & C_B & C_A \bar{X} Y \\ C_A X \bar{Y} & C_A Y & C_B \end{pmatrix} \quad (\text{C3})$$

for the partially bearded edge.

At resonant frequency $\omega_0 = 1/\sqrt{(2C_A + C_B)L}$, the diagonal element h_0 vanishes, and the Hamiltonian can be simplified as

$$\mathcal{H} = -\omega_0 \begin{pmatrix} 0 & Q_{\mathbf{k}} \\ Q_{\mathbf{k}}^\dagger & 0 \end{pmatrix}, \quad (\text{C4})$$

where $Q_{\mathbf{k}}$ is $Q_{\mathbf{k}}^I$ [Eq. (C2)] for the molecule-zigzag edge and $Q_{\mathbf{k}}^{II}$ [Eq. (C3)] for the partially bearded edge.

Regarding the momentum \mathbf{k} parallel to the unit vector \mathbf{a}_1 defined as a free parameter k_{\parallel} , the system can be viewed as an effective one-dimensional model, to which one can assign the winding number as

$$n(k_{\parallel}) = -\frac{1}{2\pi} \oint \frac{d}{dk_{\perp}} \arg(\det Q_{k_{\parallel}, k_{\perp}}) dk_{\perp}. \quad (\text{C5})$$

For $k_{\parallel} = 0$, the mirror symmetry with the mirror plane perpendicular to \mathbf{a}_1 enables us to decompose the Hamiltonian (C4) into even and odd sectors $H_{k_{\perp}^{\pm}}$, where \mathbf{k} is replaced by k_{\perp} (perpendicular to \mathbf{a}_1). Concretely, $Q_{\mathbf{k}}$ can be decomposed into even and odd sectors $Q_{k_{\perp}^{\pm}}$. Then, we can assign winding numbers for the even and odd sectors separately by substituting

$Q_{k_{\perp}^+}$ and $Q_{k_{\perp}^-}$ into Eq. (C5), which constitutes the mirror winding number (n_+ , n_-) [15].

At $k_{\parallel} = 0$, $Q_{\mathbf{k}}^I$ is decomposed into

$$Q_{k_{\perp}^+}^I = \begin{pmatrix} C_B \bar{Y}^2 & \sqrt{2}C_A \\ \sqrt{2}C_A & C_A + C_B Y \end{pmatrix}, \quad Q_{k_{\perp}^-}^I = C_B Y - C_A \quad (\text{C6})$$

by a unitary transformation $Q_{k_{\perp}^{\pm}} = \eta^{-1} Q_{\mathbf{k}} \eta$, with η being

$$\eta = \begin{pmatrix} 1 & 0 & 0 \\ 0 & \frac{\sqrt{2}}{2} & \frac{\sqrt{2}}{2} \\ 0 & \frac{\sqrt{2}}{2} & -\frac{\sqrt{2}}{2} \end{pmatrix}. \quad (\text{C7})$$

Similarly, $Q_{\mathbf{k}}^{II}$ is decomposed into even and odd sections:

$$Q_{k_{\perp}^+}^{II} = \begin{pmatrix} C_B & \sqrt{2}C_A \\ \sqrt{2}C_A \bar{Y} & C_B + C_A Y \end{pmatrix}, \quad Q_{k_{\perp}^-}^{II} = C_B - C_A Y. \quad (\text{C8})$$

Using Eq. (C5), we can compute the mirror winding number (n_+ , n_-) immediately, with the results plotted in Fig. 9(b). For circuits with molecule-zigzag and partially bearded edges, the topological edge states appear in the regions of $C_A/C_B < 1$ and $C_A/C_B > 1$, respectively.

APPENDIX D: ANALOGY TO THE QUANTUM SPIN HALL PHYSICS

In this Appendix, we clarify the meaning of the pseudospin and map our six-band Hamiltonian to the four-band Bernevig-Hughes-Zhang (BHZ) model for CdTe/HgTe/CdTe quantum wells.

Taking the molecule-zigzag unit cell as an example, we can write the Hamiltonian of an infinite Kekulé circuit at resonant frequency as

$$\mathcal{H} = -\omega_0 C_A \sum_{\langle i, j \rangle} c_i^\dagger c_j - \omega_0 C_B \sum_{\langle i', j' \rangle} c_{i'}^\dagger c_{j'}, \quad (\text{D1})$$

where c_i is the annihilation operator at site i and $\langle i, j \rangle$ and $\langle i', j' \rangle$ run over nearest-neighbor sites inside and between hexagonal unit cells, respectively. Considering a single hexagonal unit cell, the Hamiltonian \mathcal{H} is given by

$$\frac{\mathcal{H}}{-\omega C_A} = \begin{pmatrix} 0 & 0 & 0 & 0 & 1 & 1 \\ 0 & 0 & 0 & 1 & 0 & 1 \\ 0 & 0 & 0 & 1 & 1 & 0 \\ 0 & 1 & 1 & 0 & 0 & 0 \\ 1 & 0 & 1 & 0 & 0 & 0 \\ 1 & 1 & 0 & 0 & 0 & 0 \end{pmatrix}. \quad (\text{D2})$$

The eigenenergies are 2, 1, 1, -1, -1, -2, with the corresponding eigenstates

$$\begin{aligned} |s\rangle &= \left[\frac{\sqrt{6}}{6}, \frac{\sqrt{6}}{6}, \frac{\sqrt{6}}{6}, \frac{\sqrt{6}}{6}, \frac{\sqrt{6}}{6}, \frac{\sqrt{6}}{6} \right], \\ |p_x\rangle &= \left[-\frac{1}{2}, 0, \frac{1}{2}, \frac{1}{2}, 0, -\frac{1}{2} \right], \\ |p_y\rangle &= \left[-\frac{\sqrt{3}}{6}, \frac{2\sqrt{3}}{6}, -\frac{\sqrt{3}}{6}, \frac{\sqrt{3}}{6}, -\frac{2\sqrt{3}}{6}, \frac{\sqrt{3}}{6} \right], \\ |d_{x^2-y^2}\rangle &= \left[\frac{\sqrt{3}}{6}, -\frac{2\sqrt{3}}{6}, \frac{\sqrt{3}}{6}, \frac{\sqrt{3}}{6}, -\frac{2\sqrt{3}}{6}, \frac{\sqrt{3}}{6} \right], \end{aligned}$$

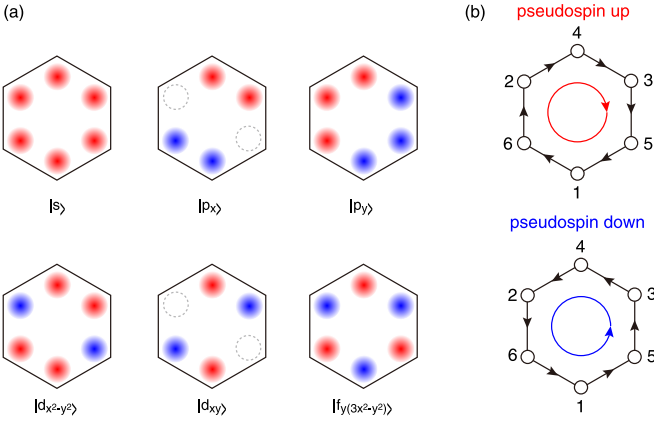


FIG. 10. (a) The orbitals in the hexagonal artificial lattice. (b) The circulating bond currents inside the unit cell. The top and bottom panels correspond to states p_+ (or d_+) and p_- (or d_-), respectively.

$$|d_{xy}\rangle = \left[\frac{1}{2}, 0, -\frac{1}{2}, \frac{1}{2}, 0, -\frac{1}{2} \right],$$

$$|f_{(3x^2-y^2)}\rangle = \left[-\frac{\sqrt{6}}{6}, -\frac{\sqrt{6}}{6}, -\frac{\sqrt{6}}{6}, \frac{\sqrt{6}}{6}, \frac{\sqrt{6}}{6}, \frac{\sqrt{6}}{6} \right],$$

respectively. They are like the s , p , d , and f atomic orbits, shown in Fig. 10(a). We can construct the following states:

$$|p_{\pm}\rangle = \frac{1}{\sqrt{2}}(|p_x\rangle \pm i|p_y\rangle),$$

$$|d_{\pm}\rangle = \frac{1}{\sqrt{2}}(|d_x\rangle \pm i|d_y\rangle), \quad (\text{D3})$$

which are related to each other by the pseudo-time-reversal (pseudo-TR) transformation $\mathcal{T} = \mathcal{U}\mathcal{K}$, with $\mathcal{U} = i\sigma_z$ (σ_z is the Pauli matrix) and \mathcal{K} being a complex conjugate operator, i.e., $\mathcal{T}|p_{\pm}\rangle = \mp i|p_{\mp}\rangle$ and $\mathcal{T}|d_{\pm}\rangle = \mp i|d_{\mp}\rangle$. $T^2 = -1$ indicates the Kramers degeneracy. It is worth mentioning that the high-energy orbits $|s\rangle$ and $|f_{(3x^2-y^2)}\rangle$ are singlets, so the pseudospin and pseudo-TR symmetry are valid only for low-energy orbits. One can straightforwardly verify that the two modes $|p_+\rangle$ and $|p_-\rangle$ ($|s_+\rangle$ and $|s_-\rangle$) are orthogonal since $\langle p_+|p_-\rangle = 0$ ($\langle s_+|s_-\rangle = 0$).

Imitating the definition of the current density for a lattice model, the bond current density between two nodes, m and n , is written as $i_{m \rightarrow n} = i(c_n^\dagger c_m - c_n c_m^\dagger)$. Using states $|p_+\rangle$ and $|p_-\rangle$ (or $|d_+\rangle$ and $|d_-\rangle$), we calculate the current distributions inside the unit cell, with the result plotted in Fig. 10(b). We find that the chiralities of the circulating currents in the unit cell are opposite, which mimics the electron spin-up and spin-down states.

Then, we downfold the six-dimensional Hamiltonian \mathcal{H} associated with the tight-binding model into the four-dimensional subspace $[p_+, d_+, p_-, d_-]$ by a unitary transformation.

For the circuit with molecule-zigzag edge geometry, we impose a unitary transformation $\mathcal{H}' = U^\dagger \mathcal{H} U$ on Hamiltonian \mathcal{H} (D1) to separate the high-energy parts of the Hamiltonian with the matrix [28]

$$U = \frac{1}{\sqrt{6}} \begin{pmatrix} e^{i\frac{\pi}{2}} & e^{i\pi} & e^{i\frac{3\pi}{2}} & e^{i\pi} & 1 & 1 \\ e^{i\frac{7\pi}{6}} & e^{i\frac{\pi}{3}} & e^{i\frac{5\pi}{6}} & e^{i\frac{5\pi}{3}} & -1 & 1 \\ e^{i\frac{11\pi}{6}} & e^{i\frac{5\pi}{3}} & e^{i\frac{\pi}{6}} & e^{i\frac{\pi}{3}} & 1 & 1 \\ e^{i\frac{\pi}{2}} & e^{i2\pi} & e^{i\frac{3\pi}{2}} & e^{i2\pi} & -1 & 1 \\ e^{i\frac{7\pi}{6}} & e^{i\frac{4\pi}{3}} & e^{i\frac{5\pi}{6}} & e^{i\frac{2\pi}{3}} & 1 & 1 \\ e^{i\frac{11\pi}{6}} & e^{i\frac{2\pi}{3}} & e^{i\frac{\pi}{6}} & e^{i\frac{4\pi}{3}} & -1 & 1 \end{pmatrix}. \quad (\text{D4})$$

Imposing Taylor expansion on each matrix element of \mathcal{H}' around the Γ point to second-order terms, we obtain

$$\mathcal{H}_\Gamma = -\omega_0 \begin{pmatrix} \delta C - \frac{9}{4}C_B k^2 & -\frac{3}{2}iC_B k_- & h_{13} & 0 & -\frac{3}{2}iC_B k_+ & h_{16} \\ \frac{3}{2}iC_B k_+ & -\delta C + \frac{9}{4}C_B k^2 & 0 & h_{24} & h_{25} & -\frac{3}{2}C_B k_- \\ h_{13} & 0 & \delta C - \frac{9}{4}C_B k^2 & -\frac{3}{2}iC_B k_+ & -\frac{3}{2}iC_B k_- & h_{36} \\ 0 & h_{24}^* & \frac{3}{2}iC_B k_- & \delta C + \frac{9}{4}C_B k^2 & h_{45} & \frac{3}{2}C_B k_+ \\ \frac{3}{2}iC_B k_- & h_{25}^* & \frac{3}{2}iC_B k_+ & h_{45}^* & -2C_A - C_B + \frac{9}{4}C_B k^2 & 0 \\ h_{16}^* & -\frac{3}{2}C_B k_+ & h_{36}^* & \frac{3}{2}C_B k_- & 0 & 2C_A + C_B - \frac{9}{4}C_B k^2 \end{pmatrix}, \quad (\text{D5})$$

with $\delta C = C_B - C_A$, $k^2 = k_x^2 + k_y^2$, $k_- = k_x - ik_y$, $h_{13} = h_{24}^* = \frac{9}{8}C_B(k_y^2 - k_x^2) - \frac{9}{4}C_B i k_x k_y$, $h_{16} = \frac{9}{8}C_B i(k_y^2 - k_x^2) - \frac{9}{4}C_B k_x k_y$, $h_{25} = h_{45}^* = \frac{9}{8}C_B(k_x^2 - k_y^2) + \frac{9}{4}C_B i k_x k_y$, and $h_{36} = \frac{9}{8}C_B i(k_x^2 - k_y^2) - \frac{9}{4}C_B k_x k_y$.

Dropping the last two high-energy orbits and the second-order off-diagonal terms h_{ij} (h_{ij} contributes as high-order perturbations), Hamiltonian (D5) is block diagonalized. We obtain the low-energy effective Hamiltonian as

$$\mathcal{H}_{\text{eff}}^1 = -\omega_0 \begin{pmatrix} \delta C - \frac{9}{4}C_B k^2 & -\frac{3}{2}iC_B k_- & 0 & 0 \\ \frac{3}{2}iC_B k_+ & -\delta C + \frac{9}{4}C_B k^2 & 0 & 0 \\ 0 & 0 & \delta C - \frac{9}{4}C_B k^2 & -\frac{3}{2}iC_B k_+ \\ 0 & 0 & \frac{3}{2}iC_B k_- & \delta C + \frac{9}{4}C_B k^2 \end{pmatrix}. \quad (\text{D6})$$

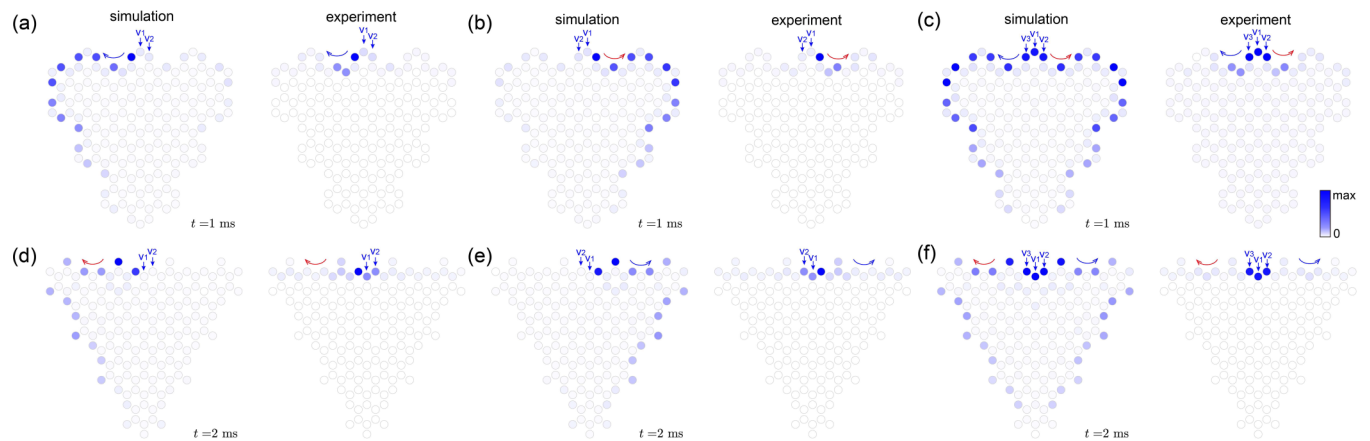


FIG. 11. (a)–(f) The simulated (left) and experimental (right) results of the propagation of the voltage with different positions of the signal sources and edge terminations.

The effective Hamiltonian $\mathcal{H}_{\text{eff}}^I$ can be rewritten in a concise BHZ form [5] as

$$\mathcal{H}_{\text{eff}}(k) = -\omega_0 \begin{pmatrix} H(k) & 0 \\ 0 & H^*(-k) \end{pmatrix}, \quad H(k) = \begin{pmatrix} M - Bk^2 & Ak_- \\ A^*k_+ & -M + Bk^2 \end{pmatrix}, \quad (\text{D7})$$

where $M = \delta C = C_B - C_A$, $A = -\frac{3}{2}iC_B$, $B = \frac{9}{4}C_B$, $k^2 = k_x^2 + k_y^2$, and $k_{\pm} = k_x \pm ik_y$.

Similarly, near the Γ point, the Hamiltonian of the partially bearded edge geometry can be simplified as

$$\mathcal{H}_{\text{eff}}^{\text{II}} = -\omega_0 \begin{pmatrix} \delta C + \frac{9}{4}C_A k_x^2 + \frac{3}{4}C_A k_y^2 & \frac{3}{2}iC_A k_- & 0 & 0 \\ -\frac{3}{2}iC_A k_+ & -\delta C - \frac{9}{4}C_A k_x^2 - \frac{3}{4}C_A k_y^2 & 0 & 0 \\ 0 & 0 & \delta C + \frac{9}{4}C_A k_x^2 + \frac{3}{4}C_A k_y^2 & \frac{3}{2}iC_A k_+ \\ 0 & 0 & -\frac{3}{2}iC_A k_- & -\delta C - \frac{9}{4}C_A k_x^2 - \frac{3}{4}C_A k_y^2 \end{pmatrix},$$

which can be rewritten as the BHZ form with

$$H(k) = -\begin{pmatrix} M - B(3k_x^2 + k_y^2) & Ak_- \\ A^*k_+ & -M + B(3k_x^2 + k_y^2) \end{pmatrix}, \quad (\text{D8})$$

where $A = -\frac{3}{2}iC_A$, $B = \frac{3}{4}C_A$, and $M = C_A - C_B$. The extra minus sign of $H(k)$ has no effect on the energy spectra because the four bands are symmetrical with respect to the zero energy. However, the opposite sign of parameter M leads to the helical edge states emerging in the opposite parameter regions for the two edge geometries.

APPENDIX E: INDEPENDENCE OF THE PSEUDOSPIN-UP AND PSEUDOSPIN-DOWN MODES

In this Appendix, we separate the pseudospin-up and pseudospin-down modes by breaking the mirror symmetry. From a mathematical point of view, the two modes are independent because the system Hamiltonian is linear. Practically, we can send only one of the two modes in our system. As shown in the left panel of Fig. 11(a), taking the molecule-zigzag edge as an example, we add two local voltage sources, $v_1(t) = v_0 \sin(\omega_0 t)$ and $v_2(t) = v_0 \sin(\omega_0 t)$, to the nodes at the boundary, indicated by two blue arrows. We then observe a unidirectional voltage propagation because the mirror symmetry of this system is broken in the presence of the two voltage sources. For comparison, we add another voltage source, $v_3(t) = v_0 \sin(\omega_0 t)$, to preserve the mirror symmetry, and the edge mode propagation becomes bidirectional [see Fig. 11(c)]. We also analyze the partially bearded case and obtain the same results [see Figs. 11(d)–11(f)]. The corresponding experimental results are displayed in the right panels

of Figs. 11(a)–11(f), and these results are fully consistent with the simulated ones.

APPENDIX F: THE RELATION BETWEEN KIRCHHOFF'S LAWS AND SCHRÖDINGER'S EQUATION

In this Appendix, we explain the relation between Kirchhoff's laws and Schrödinger's equation and calculate the admittance spectrum as well as the frequency spectrum.

In a circuit, the equation of motion is given by

$$\frac{d\mathbf{I}(t)}{dt} = C \frac{d^2\mathbf{V}(t)}{dt^2} + L\mathbf{V}(t), \quad (\text{F1})$$

where \mathbf{V} is the N -component voltage measured at each node against the ground and \mathbf{I} is the N -component input current at each node.

The homogeneous equations of motion ($\mathbf{I} = 0$) can be rewritten as $2N$ differential equations of the first order [24]:

$$-i \frac{d}{dt} \psi(t) = \mathcal{H}_S \psi(t), \quad (\text{F2})$$

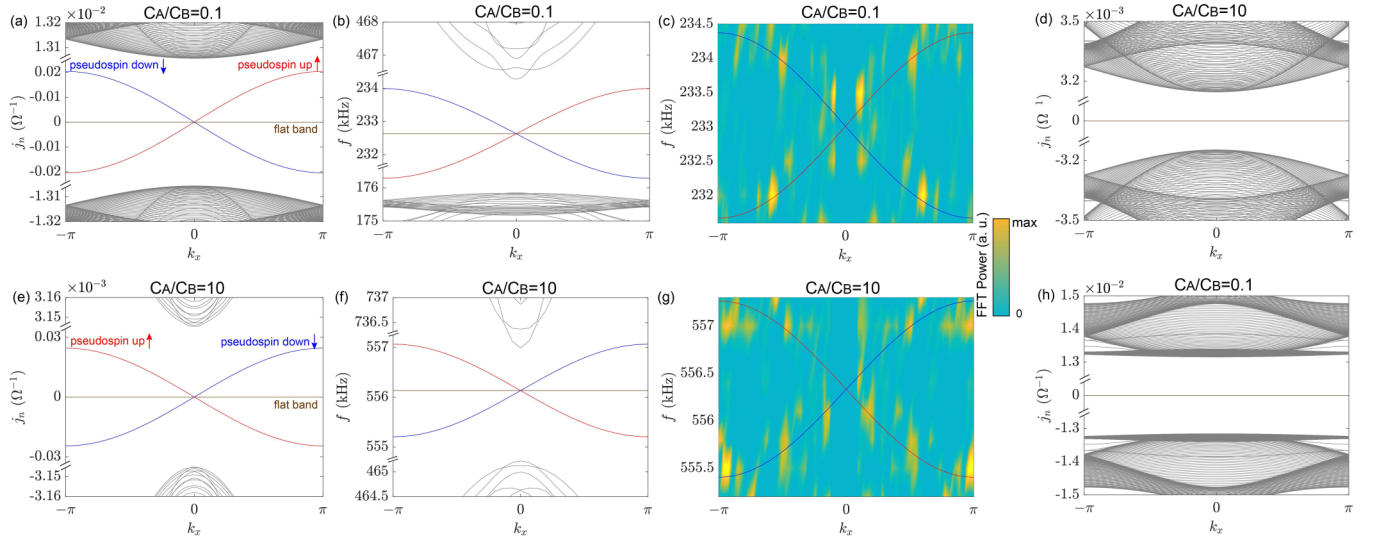


FIG. 12. (a) and (e) The admittance spectrum and (b) and (f) the frequency spectrum of the ribbon with a molecule-zigzag edge (top) and a graphene-zigzag edge (bottom). Red and blue lines represent the dispersive edge states with pseudospin up and down counterpropagating along the top edge. The brown line denotes the localized mode in the bottom boundary. (c) and (g) Experimentally measured frequency band structures near the resonant frequency ω_0 . The admittance of the ribbon with (d) capacitor ratio $C_A/C_B = 10$ and (h) $C_A/C_B = 0.1$.

with $\psi = (\dot{\mathbf{V}}(t), \mathbf{V}(t))^T$ and the Hamiltonian block matrix being

$$\mathcal{H}_S = i \begin{pmatrix} 0 & C^{-1}L \\ -1 & 0 \end{pmatrix}.$$

By diagonalizing \mathcal{H}_S , we can obtain the spectrum. The frequency-domain band structure $\omega(k_x)$ close to the resonant point ω_0 is obtained from a numerical calculation similar to that for the circuit Laplacian [see Figs. 12(a), 12(e) and 12(b), 12(f)]. We also experimentally measure the crossing frequency spectrum near the resonant frequency ω_0 , as shown in Figs. 12(c) and 12(g). The experimental results are obtained by measuring the voltage propagation at different driving frequencies (with the help of negative resistance) and imposing

a fast Fourier transform on the signal $v(x)$. Figures 12(d) and 12(h) show the admittance band structures of the trivial states for the two different edge terminations.

APPENDIX G: APPLICATIONS OF THE EDGE-DEPENDENT QUANTUM PSEUDOSPIN HALL EFFECT

In this Appendix, we introduce the potential applications of the edge-dependent quantum pseudospin Hall effect. First, the helical edge state can direct the voltage signal from one node to another, which can be used to realize information transmission, patterned imaging, and computing [see Figs. 13(a) and 13(b)]. Then, the edge-dependent effect can be used to control the signal propagation by modifying the edge shape [see Figs. 13(c) and 13(d)].

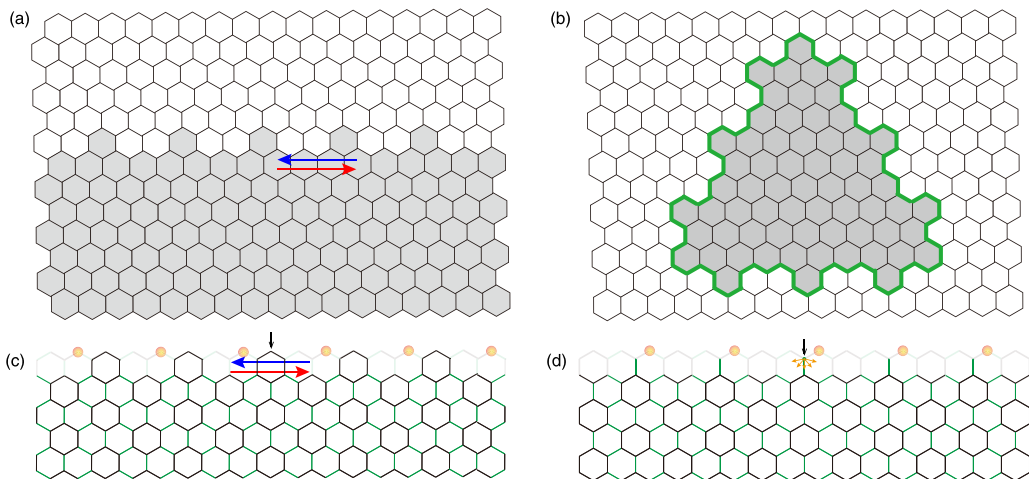


FIG. 13. (a) The voltage signal propagates along the channel between two topologically distinctive regions. (b) The patterned imaging with the topological boundary mode. Changing the sample edge from zigzag (with gray elements) to (c) molecule-zigzag and (d) partially bearded edges, the localized states (indicated by the colored balls) transform into the helical edge state and bulk state, respectively ($C_A/C_B < 1$).

- [1] M. Z. Hasan and C. L. Kane, Colloquium: Topological insulators, *Rev. Mod. Phys.* **82**, 3045 (2010).
- [2] X.-L. Qi and S.-C. Zhang, Topological insulators and superconductors, *Rev. Mod. Phys.* **83**, 1057 (2011).
- [3] C. L. Kane and E. J. Mele, Quantum Spin Hall Effect in Graphene, *Phys. Rev. Lett.* **95**, 226801 (2005).
- [4] C. L. Kane and E. J. Mele, Z_2 Topological Order and the Quantum Spin Hall Effect, *Phys. Rev. Lett.* **95**, 146802 (2005).
- [5] B. A. Bernevig, T. L. Hughes, and S.-C. Zhang, Quantum spin hall effect and topological phase transition in HgTe quantum wells, *Science* **314**, 1757 (2006).
- [6] M. König, S. Wiedmann, C. Brüne, A. Roth, H. Buhmann, L. W. Molenkamp, X.-L. Qi, and S.-C. Zhang, Quantum spin hall insulator state in HgTe quantum wells, *Science* **318**, 766 (2007).
- [7] M. König, M. Baenninger, A. G. F. Garcia, N. Harjee, B. L. Pruitt, C. Ames, P. Leubner, C. Brüne, H. Buhmann, L. W. Molenkamp, and D. Goldhaber-Gordon, Spatially Resolved Study of Backscattering in the Quantum Spin Hall State, *Phys. Rev. X* **3**, 021003 (2013).
- [8] P. Roushan, J. Seo, C. V. Parker, Y. S. Hor, D. Hsieh, D. Qian, A. Richardella, M. Z. Hasan, R. J. Cava, and A. Yazdani, Topological surface states protected from backscattering by chiral spin texture, *Nature (London)* **460**, 1106 (2009).
- [9] H. Chen, H. Nassar, A. N. Norris, G. K. Hu, and G. L. Huang, Elastic quantum spin Hall effect in kagome lattices, *Phys. Rev. B* **98**, 094302 (2018).
- [10] A. Roth, C. Brüne, H. Buhmann, L. W. Molenkamp, J. Maciejko, X.-L. Qi, and S.-C. Zhang, Nonlocal transport in the quantum spin Hall state, *Science* **325**, 294 (2009).
- [11] C. Brüne, A. Roth, H. Buhmann, E. M. Hankiewicz, L. W. Molenkamp, J. Maciejko, X.-L. Qi, and S.-C. Zhang, Spin polarization of the quantum spin Hall edge states, *Nat. Phys.* **8**, 485 (2012).
- [12] S. Hart, H. Ren, T. Wagner, P. Leubner, M. Mühlbauer, C. Brüne, H. Buhmann, L. W. Molenkamp, and A. Yacoby, Induced superconductivity in the quantum spin Hall edge, *Nat. Phys.* **10**, 638 (2014).
- [13] S. Wu, V. Fatemi, Q. D. Gibson, K. Watanabe, T. Taniguchi, R. J. Cava, and P. Jarillo-Herrero, Observation of the quantum spin Hall effect up to 100 kelvin in a monolayer crystal, *Science* **359**, 76 (2018).
- [14] S. E. Freeney, J. J. van den Broeke, A. J. J. Harsveld van der Veen, I. Swart, and C. M. Smith, Edge-Dependent Topology in Kekulé Lattices, *Phys. Rev. Lett.* **124**, 236404 (2020).
- [15] T. Kariyado and X. Hu, Topological states characterized by mirror winding numbers in graphene with bond modulation, *Sci. Rep.* **7**, 16515 (2017).
- [16] L. Fu, Topological Crystalline Insulators, *Phys. Rev. Lett.* **106**, 106802 (2011).
- [17] R.-J. Slager, A. Mesaros, V. Juričić, and J. Zaanen, The space group classification of topological band-insulators, *Nat. Phys.* **9**, 98 (2013).
- [18] T. Cao, F. Zhao, and S. G. Louie, Topological Phases in Graphene Nanoribbons: Junction States, Spin Centers, and Quantum Spin Chains, *Phys. Rev. Lett.* **119**, 076401 (2017).
- [19] Y.-L. Lee, F. Zhao, T. Cao, J. Ihm, and S. G. Louie, Topological phases in cove-edged and chevron graphene nanoribbons: Geometric structures, Z_2 invariants, and junction states, *Nano Lett.* **18**, 7247 (2018).
- [20] J.-W. Ryu, S. Woo, N. Myoung, and H. C. Park, Topological edge states in bowtie ladders with different cutting edges, *Phys. E Low-dimens. Syst. Nanostruct.* **114941** (2021).
- [21] Y. Yang, J. Lu, M. Yan, X. Huang, W. Deng, and Z. Liu, Hybrid-Order Topological Insulators in a Phononic Crystal, *Phys. Rev. Lett.* **126**, 156801 (2021).
- [22] C. H. Lee, S. Imhof, C. Berger, F. Bayer, J. Brehm, L. W. Molenkamp, T. Kiessling, and R. Thomale, Topolectrical circuits, *Commun. Phys.* **1**, 39 (2018).
- [23] S. Imhof, C. Berger, F. Bayer, J. Brehm, L. W. Molenkamp, T. Kiessling, F. Schindler, C. H. Lee, M. Greiter, T. Neupert, and R. Thomale, Topolectrical-circuit realization of topological corner modes, *Nat. Phys.* **14**, 925 (2018).
- [24] T. Hofmann, T. Helbig, C. H. Lee, M. Greiter, and R. Thomale, Chiral Voltage Propagation and Calibration in a Topolectrical Chern Circuit, *Phys. Rev. Lett.* **122**, 247702 (2019).
- [25] W. Zhu, Y. Long, H. Chen, and J. Ren, Quantum valley Hall effects and spin-valley locking in topological Kane-Mele circuit networks, *Phys. Rev. B* **99**, 115410 (2019).
- [26] Y. Lu, N. Jia, L. Su, C. Owens, G. Juzeliūnas, D. I. Schuster, and J. Simon, Probing the Berry curvature and Fermi arcs of a Weyl circuit, *Phys. Rev. B* **99**, 020302(R) (2019).
- [27] Y. Yang, D. Zhu, Z. H. Hang, and Y. D. Chong, Observation of antichiral edge states in a circuit lattice, *Sci. China Phys. Mech. Astron.* **64**, 257011 (2021).
- [28] H. Yang, Z.-X. Li, Y. Liu, Y. Cao, and P. Yan, Observation of symmetry-protected zero modes in topolectrical circuits, *Phys. Rev. Res.* **2**, 022028(R) (2020).
- [29] L. Song, H. Yang, Y. Cao, and P. Yan, Realization of the square-root higher-order topological insulator in electric circuits, *Nano Lett.* **20**, 7566 (2020).
- [30] M. Ezawa, Braiding of Majorana-like corner states in electric circuits and its non-Hermitian generalization, *Phys. Rev. B* **100**, 045407 (2019).
- [31] M. Ezawa, Electric circuits for non-Hermitian Chern insulators, *Phys. Rev. B* **100**, 081401(R) (2019).
- [32] LTSPICE, <https://www.linear.com/LTspice>.
- [33] I. Tamm, Über eine mögliche Art der elektronenbindung an kristalloberflächen, *Phys. Z. Sowjetunion* **76**, 849 (1932).
- [34] W. Shockley, On the surface states associated with a periodic potential, *Phys. Rev.* **56**, 317 (1939).
- [35] Y. Zhang, J.-P. Hu, B. A. Bernevig, X. R. Wang, X. C. Xie, and W. M. Liu, Quantum blockade and loop currents in graphene with topological defects, *Phys. Rev. B* **78**, 155413 (2008).
- [36] Y. Zhang, J.-P. Hu, B. A. Bernevig, X. R. Wang, X. C. Xie, and W. M. Liu, Localization and the Kosterlitz-Thouless Transition in Disordered Graphene, *Phys. Rev. Lett.* **102**, 106401 (2009).
- [37] L.-H. Wu and X. Hu, Topological properties of electrons in honeycomb lattice with detuned hopping energy, *Sci. Rep.* **6**, 24347 (2016).
- [38] M. Fujita, K. Wakabayashi, K. Nakada, and K. Kusakabe, Peculiar localized state at zigzag graphite edge, *J. Phys. Soc. Jpn.* **65**, 1920 (1996).